
Proceedings Paper:
Da Veiga, T, Chandler, JH, Pittiglio, G et al. (2021) Material Characterization for Magnetic Soft Robots. In: 2021 IEEE 4th International Conference on Soft Robotics (RoboSoft). 2021 IEEE 4th International Conference on Soft Robotics (RoboSoft), 12-16 Apr 2021, New Haven, CT, USA. IEEE, pp. 335-342. ISBN: 978-1-7281-7714-4.

https://doi.org/10.1109/robosoft51838.2021.9479189

Material Characterization for Magnetic Soft Robots

Tomás da Veiga[1], James H. Chandler[1], Giovanni Pittiglio[1], Peter Lloyd[1], Mohammad Holdar[2], Onaizah Onaizah[1], Ali Alazmani[2], Pietro Valdastri[1]

***Abstract*— Magnetic soft robots are increasingly popular as they provide many advantages such as miniaturization and tetherless control that are ideal for applications inside the human body or in previously inaccessible locations.**

While non-magnetic elastomers have been extensively characterized and modelled for optimizing the fabrication of soft robots, a systematic material characterization of their magnetic counterparts is still missing. In this paper, commonly employed magnetic materials made out of Ecoflex™ 00-30 and Dragon Skin™ 10 with different concentrations of NdFeB microparticles were mechanically and magnetically characterized. The magnetic materials were evaluated under uniaxial tensile testing and their behavior analyzed through linear and hyperelastic model comparison. To determine the corresponding magnetic properties, we present a method to determine the magnetization vector, and magnetic remanence, by means of a force and torque load cell and large reference permanent magnet; demonstrating a high level of accuracy. Furthermore, we study the influence of varied magnitude impulse magnetizing fields on the resultant magnetizations. In combination, by applying improved, material-specific mechanical and magnetic properties to a 2-segment discrete magnetic robot, we show the potential to reduce simulation errors from 8.5% to 5.4%.

***Index Terms*— Soft Robot Materials and Design; Modeling, Control, and Learning for Soft Robots; Surgical Robotics: Steerable Catheters/Needles**

I. Introduction

The field of soft robots has drawn considerable attention over the past years, due to the wide range of potential applications enabled through the controlled use of highly compliant materials; several examples have been reported from minimally invasive surgical procedures to common grippers [1]–[3]. Recently, the specific use of magnetic actuation in soft robots has allowed new possibilities given their advantages such as miniaturization and untethered control. From flexible soft catheters [4]–[7] to micro-robots with a wide range of locomotion capabilities [8]–[10], soft magnetic robots have gained increased attention from the robotics research community [11].

Mainly two types of magnetic soft robots have been reported [12]: those with embedded magnets within the elastomeric matrix [4], [13], [14], and those which make use of magnetic responsive elastomers (MRE) [5], [6], [8]–[10]. MRE are commonly achieved by mixing magnetic nano- or micro-particles within the elastomeric matrix and, hence, combine the elastic properties of the elastomer matrix with the magnetic properties of the particles [15], [16]. Embedding a magnetic moment is achieved via applying a strong magnetizing field, either through an impulse magnetizer [5], [17], [18] or a permanent magnet (PM) set up [10]. Impulse magnetizers offer advantages to the robotics community such as readiness, off-the-shelf and instant magnetization, over PM set-ups which cannot be switched off. Nonetheless, the resulting magnetization from impulse magnetizers obey the skin effect, in which its value decreases in depth from the objects surface inwards [19].

To achieve precise modeling, actuation and control, soft robots rely on accurate material characterizations. Considerable efforts have been made to mechanically characterize frequently employed non-magnetic elastomers [20]–[22]. However, characterization of MRE is often restricted to their microstructure and particle behaviour [23]–[25], or to their magnetorheological properties [26], [27]; which fails to provide macro-level properties of interest from a robotics point of view [16]. Furthermore, these tend to pertain to elastomers and magnetic particles that are not common within the soft robotics community due to either higher stiffness or softer magnetic properties.

Several methods for determining materials' magnetic properties have been proposed and can be broadly classified into torque and force measurements (such as Torquemeter [28] and Faraday balance [29]); magnetometric measurements (Hall probe [30], [31]); inductive measurements (vibrating sample magnetometer (VSM) [18]); and magneto-optical (e.g. MagView (Matesy GmbH, Germany)) [10], [32], [33]. These techniques can be used to determine different material aspects, and overall are able to provide an exhaustive and highly accurate analysis. However, they come with their own limitations. Torque measurements are often restricted to spherical shaped samples. Magnetometric and inductive measurements, despite allowing sample shape freedom, require small and short samples [32]. Furthermore, static inductive measurements are only capable of performing relative measurements requiring a well-defined reference. Magneto-optical measurements are limited to surface properties, being unable to provide a characterization for the whole sample directly [34]. The requirement of specific sample designs and sizes, as well as limited access to such equipment, often leads to robotic applications using properties based either on the manufacturer's data or models applied to raw materials [5], [9].

To address this, we provide a material characterization of MRE commonly employed in soft robots [5], [18], from mechanical and magnetic perspectives. Two different elas-

[1] STORM Lab, Institute of Robotics, Autonomous Systems and Sensing, School of Electronic and Electrical Engineering, University of Leeds, Leeds, UK.

[2] Surgical Technologies Lab, School of Mechanical Engineering, University of Leeds, UK.

tomeric matrices with increasing concentrations of magnetic filler are characterized. For mechanical characterization we consider a tensile analysis of these different MRE and the suitability of linear elastic and commonly employed hyperelastic models to represent their behavior. For magnetic characterization we present an easily implemented, cost-effective method for determining the magnetic moment of MRE samples. The method uses a load cell for measurements, not needing expensive single purposed magnetic specific equipment, and was used to study the influence of particle concentration, impulse magnetizing fields, and MRE stiffness on the resulting MRE magnetic moment. The results were then applied on two types of soft magnetic continuum robots to demonstrate the influence of robot-specific mechanical and magnetic characterization on simulation results.

II. Fabrication of magnetic soft material

In the present study, we consider the elastomers Ecoflex™ 00-30 (Smooth-On, Inc., U.S.A.) and Dragon Skin™ 10 (Smooth-On, Inc., U.S.A.), with all samples fabricated via molding techniques. To fabricate samples, the two-part elastomer was mixed in equal weights, followed by addition of the corresponding weight of hard magnetic micro-particles (NdFeB with an average 5 μm diameter and intrinsic coercivity of $H_{ci} = 9.65$ kOe, MQFP-B+, Magnequench GmnH, Germany). The mixture was then placed in a high vacuum-mixer (ARV-310, THINKYMIXER, Japan) for 90 seconds at a speed of 1400 rpm and pressure of 20.0 kPa and injected into the desired molds. Samples for the mechanical characterization were molded into dumbbell shape (type 2 on ISO 37:2917 [35]), whereas samples for the magnetization test were molded into cuboid shape of dimensions $7.5 \times 7.5 \times 4.0$ mm. The MRE were left to fully cure at room temperature before demolding. The samples for magnetic characterization were magnetized after curing under a magnetizing field B_m of 2.7 T or 5.0 T using an impulse magnetizer (IM-10-30, ASC Scientific, U.S.A.).

NdFeB concentrations were increased in 50% by weight increments up to the maximum supported by the elastomer matrix as listed in Table I. Concentrations above those listed prohibited curing as thus were not considered in the study.

TABLE I
Samples fabricated for characterization.

Elastomer	**Con. (wt%)**
Ecoflex™ 00-30	0
	50
	100
	150
Dragon Skin™ 10	0
	50
	100

III. Mechanical characterization

Destructive uniaxial tensile testing was applied to the different MRE samples. Their stress-strain responses were evaluated using a linear model, as well as commonly employed hyperelastic models.

A. Methods

The tensile test conditions were in accordance with ISO 37:2017 [35], using an Instron 5943 machine associated with a video-extensometer to record the elongation of the specimen. The markers for the video-extensometer were placed at 8 mm from the centre line of the specimen, and the pressure on the grippers was 20 psi. The experiments were run with a velocity of 500 mm/min until rupture. Five specimens for each type of MRE were tested.

The response of each MRE was evaluated by fitting a linear elastic model at 100% strain for all samples and retrieving the corresponding Young's modulus. Additionally, to understand the best modeling practices for MRE, a linear elastic model, and the hyperelastic models Mooney-Rivlin [37], Neo-Hookean [38], Ogden with three coefficients [39], Polynomial with 5 coefficients [40], and Yeoh [41] were fitted to the whole strain range of the obtained stress-strain curves. This was performed using a nonlinear least-squares solver from MATLAB (*lsqnonlin* function, MathWorks® Inc., U.S.A.).

B. Results and Discussion

Fig. 1 shows the stress-strain curves obtained for the different MRE, as well as the linear fits up to 100% strain. Table II lists the values of Young's modulus at 100% strain, as well as the mean absolute percentage errors (MAPE) of the linear and hyperelastic models for the whole strain range. Fig. 2 shows the fittings for the linear and hyperelastic models for the whole strain range for a sample of Ecoflex™ 00-30 and a sample of Dragon Skin™ 10 at 0 wt% NdFeB.

For both MRE, an increase in concentration of NdFeB microparticles increases the measured stress for a given strain, representing a stiffening of the composites. In fact, a concentration of only 50 wt% NdFeB results in an increase of the Young's modulus by approximately 70% for both MRE. Ecoflex™ 00-30 allows high concentrations of NdFeB up to its maximum of 150 wt%. However, the rate of increase of the Young's modulus decreases as the concentration goes up. In fact, from 100 wt% to 150 wt%, an increase of only 26% is evident. Conversely, Dragon Skin™ 10 can only withstand a maximum concentration of 100 wt%. Nonetheless, only a small increase in stiffness exists when compared to a concentration of 50 wt%. This could have certain advantages as it would lead to higher magnetic volume while maintaining the mechanical properties of lower concentrations.

The addition of NdFeB microparticles also translates to a loss of hyperelasticity. This can be easily observed in the stress-strain curves in Fig. 1; as well as the lower fitting errors for the linear model as the concentration increases in Table II. This loss of hyperelasticity is most significant for larger strains, where MRE with higher concentrations start to

TABLE II

RESULTS OF MODEL FITTING TO MRE TENSILE TEST DATA: SHOWING THE VALUES OF YOUNG'S MODULUS (E) FOR FITTING UP TO 100% STRAIN, AND THE MEAN ABSOLUTE PERCENTAGE ERROR (MAPE) FOR ALL FITTED MODELS.

		Linear model			Hyperelastic models				
		100% strain		Full strain	Neo-Hookean	Mooney-Rivlin	Yeoh	Ogden	Polynomial
Elastomer	**Con. (wt%)**	**E [kPa]**	**MAPE [%]**	**MAPE [%]**	**MAPE [%]**	**MAPE [%]**	**MAPE [%]**	**MAPE [%]**	**MAPE [%]**
Ecoflex™ 00-30	0	42.7 ± 3.9	28.7	98.0	23.0	12.2	13.2	4.8	6.5
	50	73.2 ± 10.2	22.9	66.8	17.2	19.7	14.9	7.1	5.0
	100	102.1 ± 7.3	17.8	15.2	18.3	10.0	11.3	4.0	5.3
	150	128.2 ± 4.6	24.6	21.6	14.5	16.2	13.6	6.5	4.9
Dragon Skin™ 10	0	201.1 ± 12.0	13.6	33.0	11.3	18.9	16.0	3.6	2.1
	50	343.2 ± 9.1	10.0	9.7	20.6	13.2	9.4	3.4	1.6
	100	360.1 ± 10.9	9.9	9.2	19.4	9.2	8.5	3.3	1.3

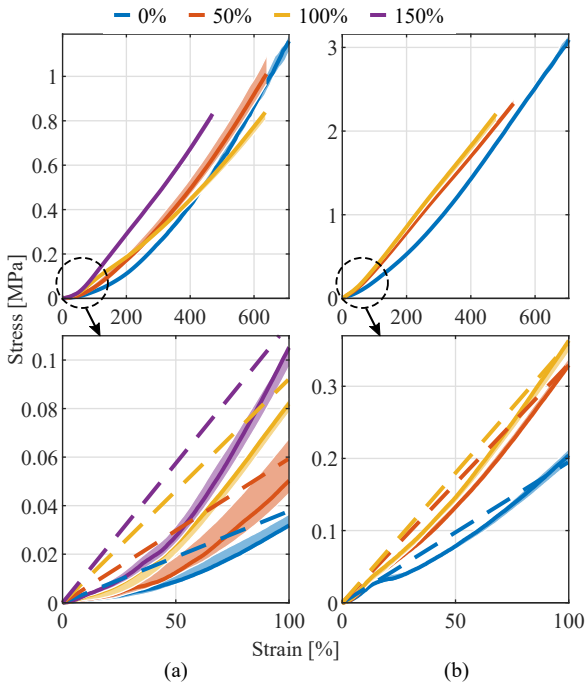

Fig. 1. Stress-Strain curves under uniaxial tensile test for (a) Ecoflex™ 00-30 and (b) Dragon Skin™ 10 with increasing concentration of NdFeB microparticles. The shaded regions define the range of values obtained for each strain across five specimens, and the full lines the values for a single sample as an example. Additionally, the dashed lines represent the fitted linear model up to 100% strain.

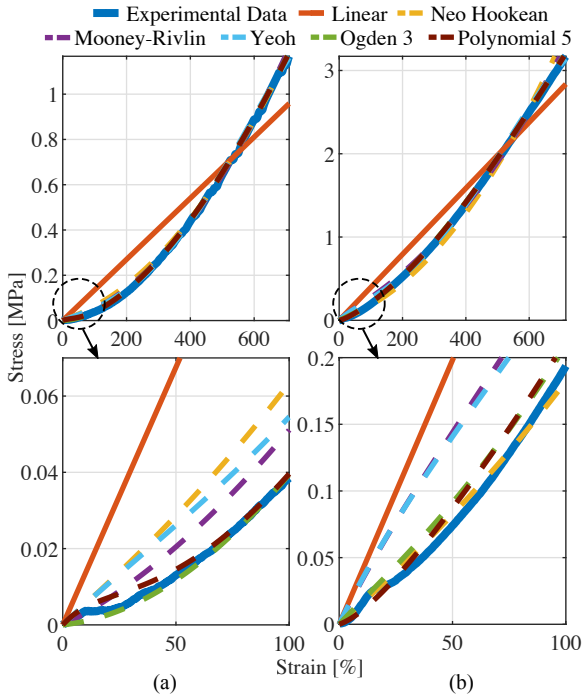

Fig. 2. (a) Ecoflex™ 00-30 at 0 wt% NdFeB and (b) Dragon Skin ™ 10 at 0 wt% NdFeB fitted with a linear elastic model and different hyperelastic models for the whole strain range.

behave linearly. Despite this, fitting errors for linear models are still higher when compared to non-linear models. Generally, the Ogden model with 3 coefficients and the Polynomial with 5 coefficients exhibit the best results with the lowest fitting errors, while the Neo-Hookean and the Mooney-Rivlin models present the highest error values. Hyperelastic models show applicability to MRE, consistently providing more accurate predictions over corresponding linear models. Still, it is expected that at the maximum limit of magnetic content, the loss of accuracy using linear models will not be as significant as for lower concentrations.

IV. MAGNETIC CHARACTERIZATION

To magnetically characterize the different MRE, the samples were placed under an external magnetic field and field gradient, and the generated forces and torques measured. This is akin to magnetically actuated soft robotic applications, where actuation and control rely on the forces and torques exerted on the robot by the external magnetic field and field gradient. By measuring the forces and torques experienced by the samples, their magnetic properties can be determined. This method was first validated on small PMs, and then used to examine the influence of particle concentration, impulse magnetizing field intensity, and MRE stiffness on the resulting MRE's magnetization.

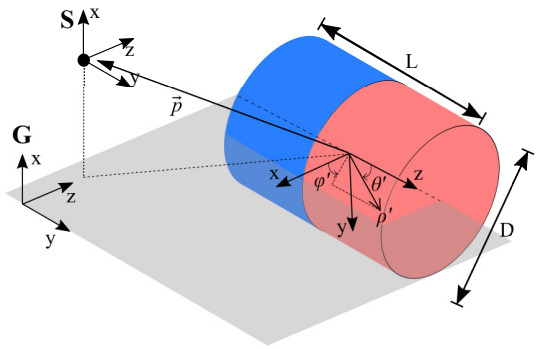

Fig. 3. Geometrical definition of variables. G denotes the global reference frame, while S the sample's frame.

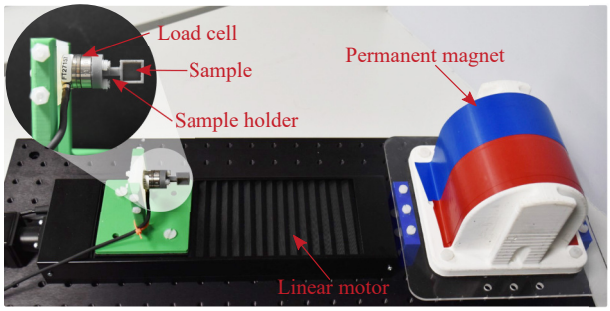

Fig. 4. Setup for the magnetic characterization of MRE.

A. Methods

1) Theoretical Background:

The magnetic force F and torque τ exerted on an object with magnetic moment m can be described by (1) and (2)

$$F = (m \cdot \nabla) B_e \tag{1}$$

$$\tau = m \times B_e \tag{2}$$

where B_e denotes the external magnetic field vector. In this work, B_e is generated by an axially magnetized cylindrical PM and is described by the following multipole expansion model in spherical coordinates [42]:

$$B_e(p) = \frac{\mu_0}{4\pi} \frac{\|m\|}{\mathrm{V}} \sum_{\mathrm{n\,odd}} \frac{\left(\frac{\mathrm{L}}{2}\right)^{\mathrm{n}+2}}{\|p\|^{\mathrm{n}+2}} \left((\mathrm{n}+1) D_{\mathrm{n}} \hat{r} - \frac{dD_{\mathrm{n}}}{d\theta} \hat{\theta} \right) \tag{3}$$

where μ_0 is the magnetic permeability of a vacuum, $\|m\|$ is the Euclidean norm of the PM's dipole moment, V the magnet's volume, L the magnet's length, p the vector from the centre of the PM to the point of interest in space, and D_n the following equation (4).

$$D_{\mathrm{n}}(\mathrm{n}, \beta) = \begin{cases} 2 \displaystyle\int_{\frac{1}{\sqrt{1+\beta^2}}}^{1} \int_{0}^{2\pi} \frac{\mathrm{P_n}(\hat{p} \cdot \hat{\rho}')}{\mathrm{x}^{\mathrm{n}+3}} \, \mathrm{d}\phi' \mathrm{dx}, & \text{if n is odd} \\ 0, & \text{if n is even} \end{cases} \tag{4}$$

where β represents the cylinder's diameter-to-length aspect ratio, and $\mathrm{P_n}(\cdot)$ the Legendre polynomial of order n [42]. Referring to Fig. 3, primed variables are defined relative to the PM for integration and all non-primed variables are defined relative to a global frame where the point of interest is defined [42].

The dipole model, which consists of the first non-zero term (i.e. $\mathrm{n} = 1$) of the previous multipole expansion model (3), is a simplifying assumption that generally yields good results for small enough samples or large enough magnet-to-magnet distances [42]. This is normally the case for situations in magnetic control or localization algorithms [43], [44]. However, for the current application where maximum accuracy is desired, the multipole expansion model with a higher number of terms provides more accurate results. Therefore, the external field was computed using the first nine non-zero terms of the multipole expansion (i.e. $\mathrm{n} = 17$); which have been reported to provide an error lower than 2% for distances greater than 1.5 minimum-bounding-sphere radii for axially magnetized cylindrical PMs with $\beta = 1$ [42].

Furthermore, B_e is a static magnetic field obeying Maxwell's equations (5) and (6).

$$\nabla \cdot \mathrm{B}_e = 0 \tag{5}$$

$$\nabla \times \mathrm{B}_e = \mu_0 \mathrm{J} \tag{6}$$

where J represents the current-density vector field, which is zero. Therefore, (1) and (2) can be rewritten as

$$\begin{bmatrix} F \\ \tau \end{bmatrix} = \begin{bmatrix} \nabla B_e \\ -B_{e\times} \end{bmatrix} m \tag{7}$$

where $(\cdot)_\times$ represents the skew operator.

Given its size, and keeping its distance from the PM large enough, the sample can be represented by a magnetic dipole. By measuring the forces and torques exerted on it, one can determine its magnetic moment using (7). Its magnetization $\mathrm{m_a}$, or magnetic remanence B_r, can then be determined via

$$\mathrm{m_a} = \frac{\|m\|}{V} \tag{8}$$

$$B_r = \frac{\|m\| \, \mu_0}{V} \tag{9}$$

2) Test rig:

The test rig can be seen in Fig. 4. It is composed of a static cylindrical N52 PM (length and diameter of 101.6 mm, axially magnetized, B_r of 1.48 T) to generate the external magnetic field and gradient. The MRE sample is attached to a 6-axis load cell (Nano17 Titanium, ATI, U.S.A.), which is mounted on a motorized linear stage (NRT150/M, Thorlabs, Inc., U.S.A.). The presence of the linear motor allows the collection of data across different values of p. The PM and the motorized stage were placed orthogonally with their centres aligned, so that the magnetic sample moves to and from the centre of the PM along the Z axis in the global coordinate frame.

For each sample, the values of force and torque were measured across 16 discrete distances, from 16 to 31 cm, centre to centre, spaced 1 cm apart. To remove noisy measurements,

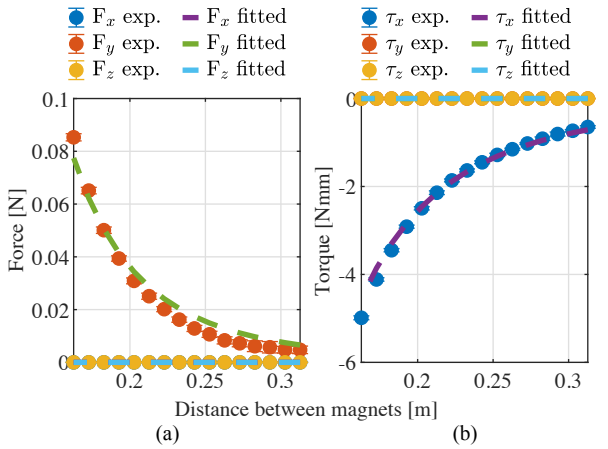

Fig. 5. (a) Force and (b) Torque measurements for a 6.35 mm cubic N52 magnet as a sample, and modelled values from fitting. MAPE 2.6%.

the difference between each two positions was averaged for each axis of the measured F and τ. In case an axis' average was below a third of the maximum average recorded, the axis was zeroed. The test was repeated three times from each sample and the average and standard deviation across repetitions computed. Points with standard deviation over a third the average force or torque were excluded. The remaining averaged data was then fitted to (7) in order to determine the values of m, using a non-linear least squares method (*lsqnonlin* function, MATLAB, MathWorks® Inc., U.S.A.).

B. Validation

The characterization approach was validated using two small PMs as samples varying in shape and size, a cubic N52 NdFeB PM of 6.35 mm length (B444-N52, K&J Magnetics Inc, U.S.A.), and a cylindrical N52 NdFeB of 3.18 mm diameter and length (D22-N52, K&J Magnetics Inc, U.S.A.). Their magnetizations were aligned with the Z axis of the global coordinate frame. Fig. 5 depicts the measured values of force and torque, against the fitted results for the cubic sample. As it can be seen, only the expected components of force and torque were activated and the measurements have very low deviation across repetitions. The B_r obtained was of 1.44 T, falling within the range expected for N52 magnets (K&J Magnetics, Inc., U.S.A.).

The current configuration works well for high remanence/large samples, such as the tested cubic PM. However, for samples with lower values, the resolution of the load cell will restrict the accuracy of the measurement. Nevertheless, one of its advantages is its flexibility to conform to specific user or equipment requirements. By varying sample size; PM size and grade; distance and relative position between PM and sample; and load cell's sensitivity, one can tailor the platform to the desired application and samples to measure.

For this specific case, force data is prone to have lower signal-to-noise ratio due to the load cell's lower force resolution when compared to torque. For that reason, only torque values can be considered in order to obtain an accurate measurement. Due to the current and fixed relative position and orientation between the PM and the sample, using only torque values hinders the possibility of obtaining the full magnetization vector. Therefore, two sample orientations were measured so that the full magnetization vector could be computed, according to (10),

$$ {}^{G}\tau = {}^{G}(-B_{\times})\ {}^{G}R_{S}\ {}^{S}m \tag{10} $$

where ${}^{G}(\cdot)$ denotes representation on the global reference frame, and ${}^{S}(\cdot)$ on the sample's reference frame, ${}^{G}R_{S}$ denotes the rotation matrix between the sample's and global reference frames. The second orientation used was 90° around the sample's y axis with respect to the first orientation. The corresponding results for the cubic and cylindrical validation PMs can be seen in Fig. 6, with remanence values of 1.46 T and 1.44 T respectively. As it can be seen, even though the torque values for the cylindrical PM are much lower, the method still gives an accurate reading of its magnetic remanence.

C. Results

1) Effect of particle concentration on MRE:
Fig. 7 depicts the values of m_a obtained for the tested MRE samples. As expected, the higher the magnetic content, the higher the value of m_a obtained. This increase of m_a with concentration is not linear as it gradually slows down as the concentration increases. In fact, for samples magnetized under $B_m = 2.7$ T, the ratio of remanence-to-concentration between 50 wt% and 100 wt% is of 0.136 T/wt%, decreasing to 0.096 T/wt% between 100 wt% and 150 wt%.

2) Effect of impulse magnetizing field intensity on MRE:
Different values of B_m gave rise to different values of m_a, even though both B_m were over the particles' intrinsic coercivity. This verifies the limitation that impulse magnetizing fields have in which the depth of penetration depends on the sample's shape and size, obeying the skin effect [19]. Therefore, even though the magnitude of B_m is more than double the intrinsic coercivity of the samples when equal to 2.7 T, it is not enough to fully magnetize the sample.

3) Effect of stiffness on MRE:
As seen in Fig. 7, no significant difference was found between Ecoflex™ 00-30 and Dragon Skin™ 10 samples. This indicates that these matrices do not affect the magnetic properties of the final MRE when submitted to a single magnetizing field. However, it has been shown that the first magnetization loop of MRE differs from the following one due to possible restructuring of the particles and elastomeric matrix, depending on the matrix's stiffness [25].

To further study this effect, samples of Ecoflex™ 00-30 and Dragon Skin™ 10 loaded at 100 wt% were submitted to two consecutive perpendicular magnetizing fields with the same previous intensities. Table III lists the average magnetization vector deviation angle with respect to the original direction. For lower impulse magnetizing fields, the resulting magnetization direction was not aligned with the magnetizing field, but at offset dependent on the MRE stiffness. The stiffer the MRE the higher the shift. When $B_m = 5$ T, the shift

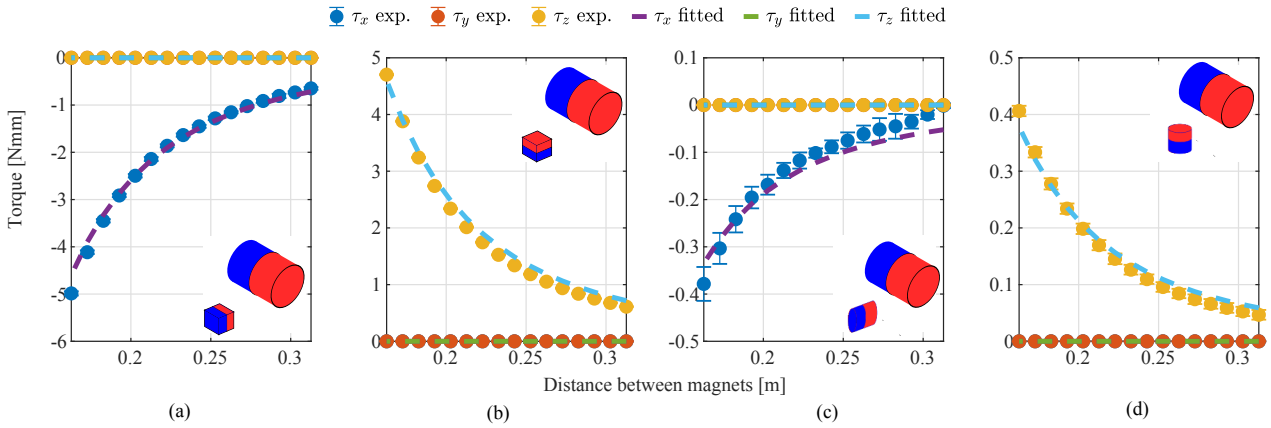

Fig. 6. Torque measurements for the validation step using permanent magnet samples, showing: cubic 6.3 mm PM (MAPE 3.1%) in (a) rotation 1, (b) rotation 2; and cylindrical 3.2 mm PM (MAPE 6.2%) in (c) rotation 1, (d) rotation 2.

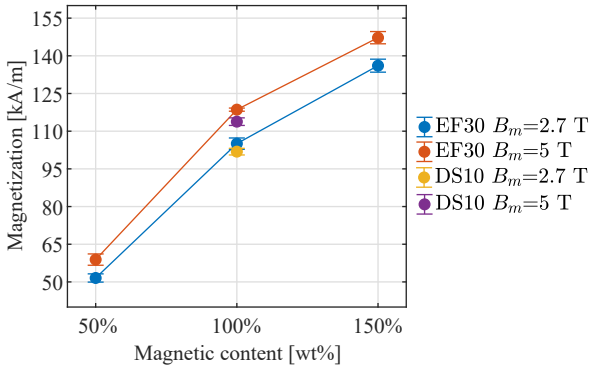

Fig. 7. Effect of the magnetic particle content and magnetizing field on the values of magnetization of MREs.

TABLE III
MAGNETIZATION VECTOR ANGLE DEVIATIONS AFTER RE-MAGNETIZATION AT A 90° ANGLE.

Elastomer	**Con. (wt%)**	$\mathbf{B_m = 2.7\ T}$	$\mathbf{B_m = 5\ T}$
Ecoflex ™ 00-30	100	55 ±1°	90 ±1°
Dragon Skin™ 10	100	61 ±1°	90 ±2°

in magnetization is complete at an average of 90° for all elastomers, indicating that high impulse magnetizing fields are able to overcome any restructuring of softer matrices and particle movement and fully re-magnetize the composite.

V. VALIDATION

To validate the characterization results, soft magnetic continuum robots were fabricated and actuated under a uniform external magnetic field. Two types of robots were studied, covering the designs showcased in the literature: fully soft magnetic robots [6] and fully soft robots with magnetic and non-magnetic regions [5]. Their behavior was then compared to the corresponding 2D finite element models (FEM) either assuming the theoretical properties or our corrected values. Both the fabrication methods and FEM have been previously described in [5].

Fig. 8 shows the results obtained for the fully soft magnetic continuum robot. The robot, which is 37 mm long and 5 mm in diameter, consists of Ecoflex™ 00-30 loaded at 100 wt% NdFeB, axially magnetized under the both previous B_m values (2.7 T and 5 T). Fig. 8(b) shows the experimental deflections obtained for both magnetizing fields. As it can be seen, the robot magnetized under 5 T exhibits a slightly larger deflection. Given that both B_m values are over the particles' intrinsic coercivity value, the theoretical magnetic remanence does not distinguish the two; assuming a value of 107 mT for both cases. Furthermore, the material is modelled linearly with a Young's modulus of 69 kPa, as per its datasheet. On the contrary, our corrected values are able to distinguish between the two different B_m, as well as provide a more accurate value of Young's modulus. This difference is enough to achieve deflections closer to the real-life results, lowering MAPE errors from 9.9% to 7.5% for $B_m = 2.7$ T, and 11.5% to 5.6% when $B_m = 5$ T. The remaining error can be further reduced by studying how the mechanical properties of the MRE change when under actuation, as well as using application specific values.

The results achieved for the fully soft discrete magnetic continuum robot are presented in Fig. 9. The robot is 40 mm long, and 3 mm in diameter. It is made of Ecoflex™ 00-30, consisting of plain sections alternated with axially magnetized 150 wt% NdFeB sections. The robot was magnetized under 5 T to achieve maximum magnetization. In this case, theoretical values are blind to mechanical differences between sections, assuming a constant Young's modulus of 69 kPa for the whole length of the robot. The corrected model, on the other hand, is able to provide a responsive value of Young's modulus with increasing concentration of NdFeB, as well as a more accurate value of magnetic remanence, lowering the MAPE error from 8.5% to 5.4%.

VI. CONCLUSIONS

In this paper, we presented a material characterization for magnetic elastomers commonly employed in soft robots that

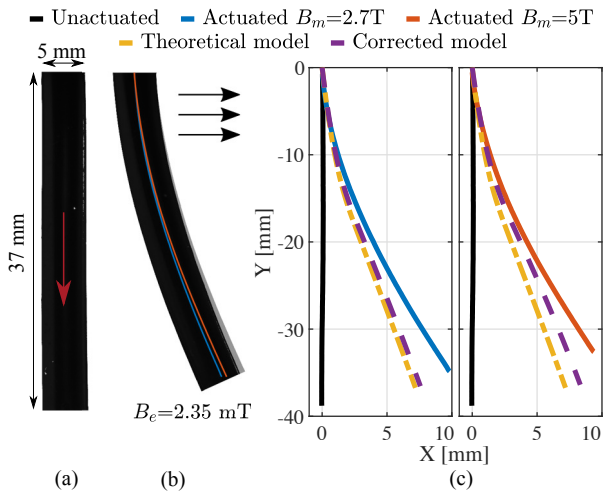

Fig. 8. (a) Fully soft magnetic continuum robot. The red arrow represents its magnetization direction. (b) The robot under actuation in an uniform magnetic field with direction represented by the black arrows. (c) Simulation results considering our corrected model and the theoretical model.

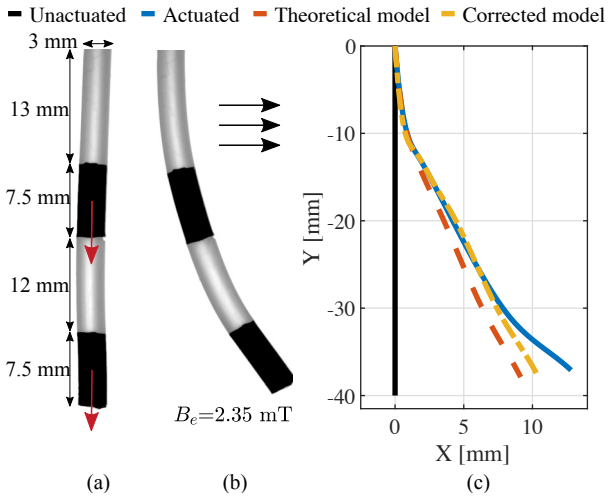

Fig. 9. (a) Fully soft discrete magnetic continuum robot. The red arrows represent the direction of magnetization. (b) The robot under actuation in an uniform magnetic field with direction represented by the black arrows. (c) Simulation results considering our correct model and the theoretical model.

is able to reduce errors in their modeling and simulation.

Tensile testing and a hyperelasticity analysis of Ecoflex™ 00-30 and Dragon Skin™ 10 showed that an increase in concentration of NdFeB content, in addition to stiffening the MRE, translates into a loss of hyperelasticity. Even so, for the majority of the cases, hyperelastic models are still able to predict the materials' behavior more accurately than linear models, especially hyperelastic models Ogden and Polynomial.

To magnetically characterize the MRE, we propose a method based on a 6 degree of freedom load cell that measures the forces and torques exerted on the sample by an external PM. One can finely tune parameters (for example the PM specifications, its distance and relative orientation to the sample, load cell's accuracy, and samples' physical size and remanence) to achieve optimal results. For example, smaller distances require less sensitive load cells and allow smaller and weaker samples, however, errors associated with the dipole assumption will increase. Larger distances, on the other hand, decrease errors from the dipole model assumption but require larger and stronger samples, and highly sensitive load cells in order to guarantee an acceptable signal-to-noise ratio. Additionally, the load cell needs to be calibrated in an external-magnetic-field-free environment before each measurement, and have minimum magnetic interferences during measurements to maximize measurement quality. The method was validated using PMs of different sizes and shapes as samples, and shown to be able to determine their magnetization vector and remanence accurately. The method was used to characterize MRE and study the effect of particle concentration, intensity of impulse magnetizing field, and elastomer stiffness on the resultant MRE magnetic properties. Higher magnetic content leads to higher magnetization non-linearly, as it slows down with concentration. Furthermore, unlike impulse fields 5.2 times the MRE intrinsic coercivity value, impulse fields 2.8 times were not able to fully magnetize the samples, reflecting the dependency on skin effect's. Matrix stiffness was shown to have an effect on the resulting magnetization direction when subjected to multiple magnetization cycles. Nevertheless, this effect is only present in lower magnetizing impulse fields.

As these factors (elasticity, magnetization value and history, and concentration of magnetic content) all influence the properties of the soft robot in interconnected and non-linear ways, having a practical method to characterize properties provides a useful tool in improved design, modeling, and simulation of magnetic soft robots. As such, these findings were subsequently validated on two types of fully soft magnetic continuum robots and shown to reduce modeling errors on average by 37% when compared to using theoretical parameters normally provided by manufacturers or parameters from raw data. This reduction can be further increased by utilizing application strain specific mechanical properties and models, testing how the mechanical properties of the MRE change when under actuation, and more repeatable and accurate soft robot fabrication methods.

ACKNOWLEDGEMENT

Research reported in this article was supported by the Royal Society, by the Engineering and Physical Sciences Research Council (EPSRC) under grant numbers EP/R045291/1 and EP/V009818/1, and by the European Research Council (ERC) under the European Union's Horizon 2020 research and innovation programme (grant agreement No 818045). Any opinions, findings and conclusions, or recommendations expressed in this article are those of the authors and do not necessarily reflect the views of the Royal Society, EPSRC, or the ERC.

REFERENCES

[1] D. Rus and M. T. Tolley, "Design, fabrication and control of soft robots," *Nature*, vol. 521, no. 7553, pp. 467–475, 2015.

[2] M. Cianchetti, T. Ranzani, G. Gerboni, T. Nanayakkara, K. Althoefer, P. Dasgupta, and A. Menciassi, "Soft robotics technologies to address shortcomings in today's minimally invasive surgery: the stiff-flop approach," *Soft robotics*, vol. 1, no. 2, pp. 122–131, 2014.

[3] G. M. Whitesides, "Soft robotics," *Angewandte Chemie International Edition*, vol. 57, no. 16, pp. 4258–4273, 2018.

[4] S. Jeon, A. K. Hoshiar, K. Kim, S. Lee, E. Kim, S. Lee, J.-y. Kim, B. J. Nelson, H.-J. Cha, B.-J. Yi *et al.*, "A magnetically controlled soft microrobot steering a guidewire in a three-dimensional phantom vascular network," *Soft robotics*, vol. 6, no. 1, pp. 54–68, 2019.

[5] P. R. Lloyd, T. Da Veiga, A. Attanasio, N. Marahrens, J. H. Chandler, P. Valdastri *et al.*, "A learnt approach for the design of magnetically actuated shape forming soft tentacle robots," *IEEE Robotics and Automation Letters*, 2020.

[6] Y. Kim, G. A. Parada, S. Liu, and X. Zhao, "Ferromagnetic soft continuum robots," *Science Robotics*, vol. 4, no. 33, p. eaax7329, 2019.

[7] P. Lloyd, G. Pittiglio, J. H. Chandler, and P. Valdastri, "Optimal design of soft continuum magnetic robots under follow-the-leader shape forming actuation," *2020 International Symposium on Medical Robotics (ISMR)*, 2020, accepted.

[8] W. Hu, G. Z. Lum, M. Mastrangeli, and M. Sitti, "Small-scale soft-bodied robot with multimodal locomotion," *Nature*, vol. 554, no. 7690, pp. 81–85, 2018.

[9] V. K. Venkiteswaran, L. F. P. Samaniego, J. Sikorski, and S. Misra, "Bio-inspired terrestrial motion of magnetic soft millirobots," *IEEE Robotics and automation letters*, vol. 4, no. 2, pp. 1753–1759, 2019.

[10] T. Xu, J. Zhang, M. Salehizadeh, O. Onaizah, and E. Diller, "Millimeter-scale flexible robots with programmable three-dimensional magnetization and motions," *Science Robotics*, vol. 4, no. 29, p. eaav4494, 2019.

[11] T. da Veiga, J. H. Chandler, P. Lloyd, G. Pittiglio, N. J. Wilkinson, A. K. Hoshiar, R. A. Harris, and P. Valdastri, "Challenges of continuum robots in clinical context: a review," *Progress in Biomedical Engineering*, vol. 2, no. 3, p. 032003, 2020.

[12] J. J. Abbott, E. Diller, and A. J. Petruska, "Magnetic methods in robotics," *Annual Review of Control, Robotics, and Autonomous Systems*, vol. 3, 2020.

[13] C. Chautems, A. Tonazzini, D. Floreano, and B. J. Nelson, "A variable stiffness catheter controlled with an external magnetic field," in *2017 IEEE/RSJ International Conference on Intelligent Robots and Systems (IROS)*. IEEE, 2017, pp. 181–186.

[14] A. J. Petruska, "Open-loop orientation control using dynamic magnetic fields," *IEEE Robotics and Automation Letters*, vol. 5, no. 4, pp. 5472–5476, 2020.

[15] M. Schümann, D. Y. Borin, S. Huang, G. K. Auernhammer, R. Müller, and S. Odenbach, "A characterisation of the magnetically induced movement of ndfeb-particles in magnetorheological elastomers," *Smart Materials and Structures*, vol. 26, no. 9, p. 095018, 2017.

[16] N. Bira, P. Dhagat, and J. R. Davidson, "A review of magnetic elastomers and their role in soft robotics," *Frontiers in Robotics and AI*, vol. 7, p. 146, 2020. [Online]. Available: https://www.frontiersin.org/article/10.3389/frobt.2020.588391

[17] R. Zhao, Y. Kim, S. A. Chester, P. Sharma, and X. Zhao, "Mechanics of hard-magnetic soft materials," *Journal of the Mechanics and Physics of Solids*, vol. 124, pp. 244–263, 2019.

[18] Y. Kim, H. Yuk, R. Zhao, S. A. Chester, and X. Zhao, "Printing ferromagnetic domains for untethered fast-transforming soft materials," *Nature*, vol. 558, no. 7709, pp. 274–279, 2018.

[19] J. Stöhr and H. C. Siegmann, "Magnetism," *Solid-State Sciences. Springer, Berlin, Heidelberg*, vol. 5, 2006.

[20] C. Schumacher, E. Knoop, and M. Bacher, "Simulation-ready characterization of soft robotic materials," *IEEE Robotics and Automation Letters*, 2020.

[21] J. C. Case, E. L. White, and R. K. Kramer, "Soft material characterization for robotic applications," *Soft Robotics*, vol. 2, no. 2, pp. 80–87, 2015.

[22] D. Steck, J. Qu, S. B. Kordmahale, D. Tscharnuter, A. Muliana, and J. Kameoka, "Mechanical responses of ecoflex silicone rubber: Compressible and incompressible behaviors," *Journal of Applied Polymer Science*, vol. 136, no. 5, p. 47025, 2019.

[23] G. Stepanov, D. Y. Borin, A. Bakhtiiarov, and P. Storozhenko, "Negative coercivity of magnetic elastomers filled with magnetically hard particles," *Journal of Magnetism and Magnetic Materials*, vol. 498, p. 166125, 2020.

[24] K. Kalina, J. Brummund, P. Metsch, M. Kästner, D. Y. Borin, J. Linke, and S. Odenbach, "Modeling of magnetic hystereses in soft mres filled with ndfeb particles," *Smart Materials and Structures*, vol. 26, no. 10, p. 105019, 2017.

[25] J. M. Linke, D. Y. Borin, and S. Odenbach, "First-order reversal curve analysis of magnetoactive elastomers," *RSC advances*, vol. 6, no. 102, pp. 100 407–100 416, 2016.

[26] W. Li, Y. Zhou, and T. Tian, "Viscoelastic properties of mr elastomers under harmonic loading," *Rheologica acta*, vol. 49, no. 7, pp. 733–740, 2010.

[27] W. Li, X. Zhang, and H. Du, "Development and simulation evaluation of a magnetorheological elastomer isolator for seat vibration control," *Journal of Intelligent Material Systems and Structures*, vol. 23, no. 9, pp. 1041–1048, 2012.

[28] A. Aldenkamp, C. Marks, and H. Zijlstra, "Frictionless recording torque magnetometer," *Review of Scientific Instruments*, vol. 31, no. 5, pp. 544–546, 1960.

[29] B. L. Morris and A. Wold, "Faraday balance for measuring magnetic susceptibility," *Review of Scientific Instruments*, vol. 39, no. 12, pp. 1937–1941, 1968.

[30] X. Granados, S. Sena, E. Bartolomé, A. Palau, T. Puig, X. Obradors, M. Carrera, J. Amorós, and H. Claus, "Characterization of superconducting rings using an in-field hall probe magnetic mapping system," *IEEE Transactions on applied superconductivity*, vol. 13, no. 2, pp. 3667–3670, 2003.

[31] M. Kustov, P. Laczkowski, D. Hykel, K. Hasselbach, F. Dumas-Bouchiat, D. O'Brien, P. Kauffmann, R. Grechishkin, D. Givord, G. Reyne *et al.*, "Magnetic characterization of micropatterned nd–fe–b hard magnetic films using scanning hall probe microscopy," *Journal of Applied Physics*, vol. 108, no. 6, p. 063914, 2010.

[32] F. Fiorillo, *Measurement and characterization of magnetic materials*. North-Holland, 2004.

[33] Y. Alapan, A. C. Karacakol, S. N. Guzelhan, I. Isik, and M. Sitti, "Reprogrammable shape morphing of magnetic soft machines," *Science Advances*, vol. 6, no. 38, p. eabc6414, 2020.

[34] A. Hubert and R. Schäfer, *Magnetic domains: the analysis of magnetic microstructures*. Springer Science & Business Media, 2008.

[35] ISO, "Rubber, vulcanized or thermoplastic — determination of tensile stress-strain properties," International Organization for Standardization, Geneva, Switzerland, ISO 37, 2017.

[36] M. Holdar, P. Culmer, and A. Alazmani, "Standardised methodology for characterization of soft elastomeric materials in soft robotics," *IEEE International Conference on Soft Robotics (RoboSoft)*, 2021, (under review).

[37] M. Mooney, "A theory of large elastic deformation," *Journal of applied physics*, vol. 11, no. 9, pp. 582–592, 1940.

[38] B. Kim, S. B. Lee, J. Lee, S. Cho, H. Park, S. Yeom, and S. H. Park, "A comparison among neo-hookean model, mooney-rivlin model, and ogden model for chloroprene rubber," *International Journal of Precision Engineering and Manufacturing*, vol. 13, no. 5, pp. 759–764, 2012.

[39] R. W. Ogden, "Large deformation isotropic elasticity–on the correlation of theory and experiment for incompressible rubberlike solids," *Proceedings of the Royal Society of London. A. Mathematical and Physical Sciences*, vol. 326, no. 1567, pp. 565–584, 1972.

[40] R. S. Rivlin and D. Saunders, "Large elastic deformations of isotropic materials vii. experiments on the deformation of rubber," *Philosophical Transactions of the Royal Society of London. Series A, Mathematical and Physical Sciences*, vol. 243, no. 865, pp. 251–288, 1951.

[41] O. H. Yeoh, "Some forms of the strain energy function for rubber," *Rubber Chemistry and technology*, vol. 66, no. 5, pp. 754–771, 1993.

[42] A. J. Petruska and J. J. Abbott, "Optimal permanent-magnet geometries for dipole field approximation," *IEEE transactions on magnetics*, vol. 49, no. 2, pp. 811–819, 2012.

[43] A. Z. Taddese, P. R. Slawinski, M. Pirotta, E. De Momi, K. L. Obstein, and P. Valdastri, "Enhanced real-time pose estimation for closed-loop robotic manipulation of magnetically actuated capsule endoscopes," *The International journal of robotics research*, vol. 37, no. 8, pp. 890–911, 2018.

[44] L. Barducci, G. Pittiglio, J. C. Norton, K. L. Obstein, and P. Valdastri, "Adaptive dynamic control for magnetically actuated medical robots," *IEEE robotics and automation letters*, vol. 4, no. 4, pp. 3633–3640, 2019.